Numerical Study of Surface Pressure Fluctuation on Rigid Disk-Gap-Band-Type Supersonic Parachutes

K. Kitamura* and K. Fukumoto†
Yokohama National University, Yokohama 240-8501, Japan
and
K. Mori‡
Nagoya University, Nagoya 464-8603, Japan

In the aerodynamic characteristics of supersonic parachutes, it is important to understand surface pressure distribution because it is strongly related to the fluctuation of drag and problematic unstable deformation of a parachute. However, there is a paucity of studies that focuses on the detailed surface pressure distribution. Therefore, we investigated the interior and exterior of a rigid disk-gap-band-type parachute as the first step, under the assumption that the forebody or suspension lines are absent, and thus the pressure and drag fluctuations are small. Two configurations are considered: one with a continuous gap and a vent orifice, representing a conventional Disk-Gap-Band parachute, and one with a discontinuous gap made up of 8 separate orifices and a vent orifice. By making the gap discontinuous, the interior and exterior pressure fluctuations are reduced. Furthermore, as indicated by the flowfield analysis, the discrete gap reduces the asymmetric pressure distribution interior the parachute, and the interior pressure fluctuation far from the center is suppressed. The result is considered useful for the suppression of unstable deformation such as area oscillation. This is currently a problem in supersonic parachute operation. In addition, we have identified locations on the model surface where the pressure fluctuations contribute to the drag fluctuations of the model.

Nomenclature

a	=	speed of sound
C_D	=	drag coefficient
C_p	=	pressure coefficient
D_p	=	projected diameter of canopy
D_V	=	vent diameter
D_0	=	nominal (reference) diameter of canopy
e_T	=	total energy per unit volume
E_k, F_k	=	inviscid and viscous flux vectors in k direction ($k = 1, 2, 3$ corresponding to to x, y, z, respectively)
H	=	total enthalpy
H_B	=	height of band
H_C	=	height of canopy
H_G	=	height of gap
M	=	Mach number
Pr	=	Prandtl number; 0.71
p	=	local pressure
p_0	=	total pressure
Q	=	conservative variable vector
q	=	primitive variable ($\rho, u, v, w,$ or p in three dimensions)
R	=	reattachment region
Re	=	Reynolds number based on 1 m and freestream speed of sound
Re_{Dp}	=	Reynolds number based on D_p and freestream velocity
S_{opening}	=	total opening area
S_G	=	gap opening area
S_p	=	projected area of canopy
S_R	=	separated region
S_t	=	stagnation region
S_V	=	vent opening area
S_0	=	nominal (reference) canopy surface area
T	=	temperature, or period of time
u_k	=	velocity components in Cartesian coordinates
V_L	=	longitudinal vortex
X_p	=	depth of cylindrical parachute model
x_k	=	Cartesian coordinates
y^+	=	nondimensional wall distance
α	=	angle of attack
γ	=	specific heat ratio; 1.4
δp	=	pressure fluctuations
κ	=	thermal conductivity; $\mu c_p / Pr$
λ_g	=	geometric porosity
μ	=	molecular viscosity
ρ	=	density
σ_{CD}	=	standard deviation of drag coefficient fluctuation
σ_p	=	standard deviation of pressure fluctuation
φ	=	azimuthal angle around x axis

Subscripts

ave	=	average value
case1	=	value of case 1
case2	=	value of case 2
i	=	cell i
i, j	=	interface between cells i and j
in	=	value inside canopy
out	=	value outside canopy
0	=	value at azimuthal angle $\varphi = 0$
22.5	=	value at azimuthal angle $\varphi = 22.5$
∞	=	freestream value

*Associate Professor, Graduate School of Engineering, 79-5 Tokiwadai, Hodogaya-ku, Kanagawa. Senior Member AIAA.
†Graduate Student, Graduate School of Engineering, 79-5 Tokiwadai, Hodogaya-ku, Kanagawa.
‡Associate Professor, Graduate School of Engineering, Furouchou, Chikusa-ku, Aichi.

I. Introduction

RECENTLY in the space development field, manned planetary exploration (especially to Mars) attracted worldwide attention. To realize future manned planetary exploration, a more reliable parachute system is necessary for landing. The disk-gap-band (DGB)-type supersonic parachute is traditionally adopted [1], and the parachute exhibits the open areas termed as the gap and vent (see Fig. 1). The flow of air from the open areas reduces the force generated during parachute

a) Case 1 (perspective view)

b) Case 2 (perspective view)

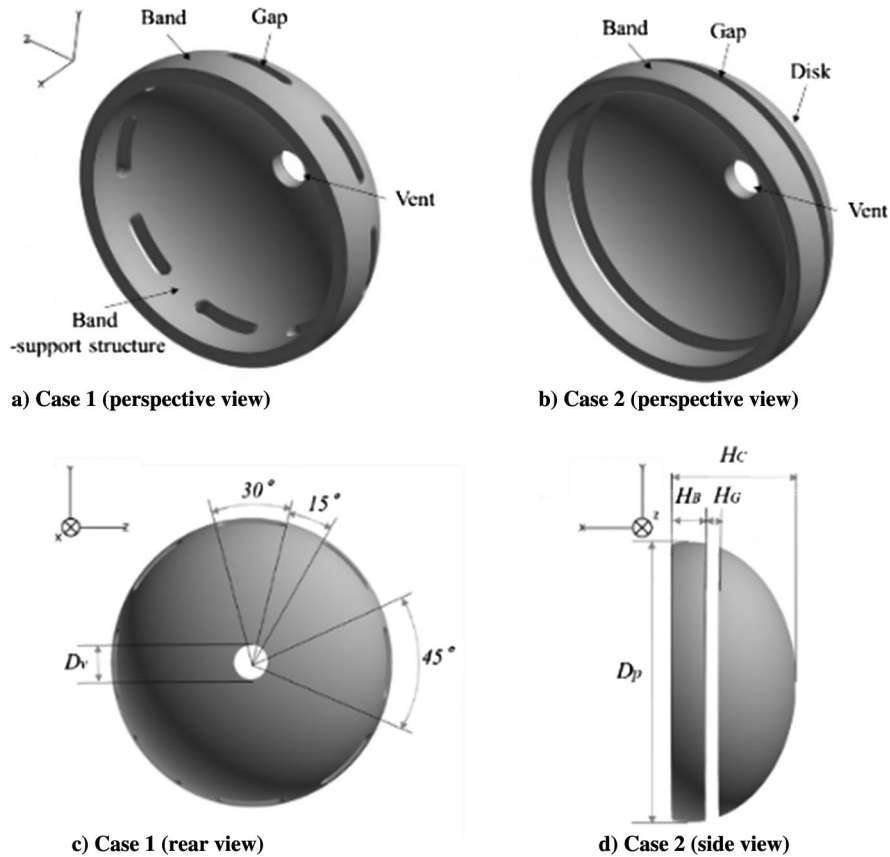c) Case 1 (rear view)

d) Case 2 (side view)

Fig. 1   Configuration.

inflation [2]. The supersonic parachute also exhibits significant advantages in terms of drag per weight and transportability, although its reliability still remains a challenge. The interaction between the wake of the payload and detached shock wave is focused on as an unstable phenomenon. With respect to the phenomenon, the conditions to avoid large-scale interference were clarified in several previous studies [3–5]. Let us briefly review the related, earlier works (computational studies are summarized in Table 1).

Karagiozis et al. [6] conducted an elaborate ghost-fluid-method-based large-eddy simulation (LES) on the Mach 2 flow around a DGB-type parachute, where the forebody and the parachute deformation were considered but permeability treatment was not clearly explained. In spite of their considerable effort, however, their solution still exhibits 20% errors compared with the corresponding experiment conducted by Sengupta et al. [7]. According to Karagiozis et al. [6], this difference arose from the poor resolution at the wake flow and the shock interaction. They also carried out the detached-eddy simulation, yielding only 3–6% differences from the LES result. In addition, they actually focused on the canopy deformation itself but did not examine the detailed wake flow dynamics. Another important work by Kim and Peskin [8] simulated flows around single and multiple parachutes using the immersed-boundary method (IBM). However, their conditions were limited to very low speed (0.6–1.2 m/s). Xue and Nakamura [9] and Xue et al. [10,11] conducted a series of studies on

supersonic parachutes. In Refs. [10,11], they assumed the parachute canopy was rigid (i.e., no deformation was considered) and focused on its surrounding supersonic flow physics, such as shock interactions and oscillations: Particular attention was paid to the separation between the forebody and the canopy in Ref. [10], whereas the effects of the (rigid-body-modeled) suspension lines were discussed in Ref. [11]. The effect of separation distance was surveyed in Ref. [9] for a flexible canopy. All these findings were of great importance, but they assumed laminar flows throughout their papers. They claimed that their solution was in good agreement with the experimental data for time-averaged surface pressure values. However, it is questionable whether turbulent effects were truly negligible in their cases, especially in terms of unsteadiness of the wake flow and the shock. Guruswamy [12] did three-degree-of-freedom (3-DOF) computations at Mach 0.43 and 2.0. However, he employed a classical numerical flux (which has huge numerical dissipation) with a Reynolds-averaged Navier–Stokes (RANS) turbulence model. Hence, the resultant flow resolution could be somewhat degraded, although the method itself was worth mentioning. Tezduyar et al. [13] also conducted a milestone work. They proposed a fluid–structure-interaction (FSI)-type method and applied it to a parachute canopy, considering its deformation, porosity, and the suspension lines. However, their flow velocity is limited to 25.7 ft/s (very low speed), which is obviously different from our target condition, i.e., an unsteady, supersonic

Table 1   Related computational parachute flow papers

Authors	Primary focus	Turbulent treatment	Mach number	Deformation treatment	Permeability	Forebody	Suspension lines/risers
Present	Wake/canopy	DDES	2	Rigid	No	No	No
Karagiozis et al. [6]	Canopy deformation	LES	2	Ghost fluid	No	Yes	Yes
Kim and Peskin [8]	Multiple parachutes	Laminar	0.002–0.004	IBM	No	No	Yes
Xue and Nakamura [9]	Canopy deformation	Laminar	1.6–2.1	IBM	No	Yes	No
Xue et al. [10]	Suspension lines	Laminar	2	Rigid/IBM	No	Yes	Yes
Xue et al. [11]	Clearance	Laminar	2	Rigid	No	Yes	No
Guruswamy [12]	Method	RANS	0.43, 2	3-DOF/damper	No	Yes	No
Tezduyar et al. [13]	Method	Laminar	0.02	FSI	Yes	No	Yes

turbulent wake flow. Moreover, the last two papers were dedicated to the proposed method therein and the demonstrations of their capabilities rather than the wake flow unsteadiness. This holds also to Stein et al.'s work [14], where fluid–structure-interaction (FSI) simulations were carried out on the parachute canopy with an apparently low flow velocity.

As indicated earlier in this paper, there is a paucity of extant studies on the supersonic DGB parachute's wake. The steady pressure distribution exterior to the canopy is examined with respect to a hemispherical cup [15] (which is a simpler form) and a flat circular ribbon parachute [16] (in which the influence on the wake is low due to a small opening area). However, the larger opening area of the DGB generates a larger jet, and the jet significantly interacts with the wake; this complicates the wake (the flow physics of such a jet formation and its shock interaction are very similar to those of crossflow jets, e.g., Refs. [17,18]). Simultaneously, the complicated wake can cause motion of the bow shock ahead of the canopy, possibly resulting in pressure changes inside the canopy and the area oscillation. To suppress the phenomenon, it is necessary to understand the basic physics of the flow around the DGB parachute. However, the wake of the DGB that is generated by the interaction between supersonic flow and a flexible body is extremely complicated [6]. To understand the complex flow, it is necessary to assume that there is no parachute deformation or no forebody (capsule ahead of the canopy). Furthermore, on the actual parachute surface, the interior and the exterior pressure fluctuations are closely related to the parachute deformation and flutter as previously described. However, it is difficult to investigate the wake in detail from the viewpoint of model support in a wind-tunnel test [7,19].

Hence, we will investigate the pressure fluctuation on the interior and exterior of a rigid model that mimics the supersonic DGB parachute by using computational fluid dynamics (CFD) as a first step to understanding the DGB wake: specifically, delayed detached-eddy simulation (DDES) [20], which captures most of the wake flows by accurate LES but switches to economical RANS at near-wall flows (and is now becoming one of the standard methods for afterbody flows [21]), will be used. Additionally, we will discuss the fundamental physics of the flow around a model representing a DGB canopy in isolation, including the relation between the surface pressure fluctuation amplitude and characteristics of the flowfield or position. Furthermore, we will select the gap configuration that significantly influences the flowfield as a parameter and compare the difference in the surface pressure fluctuation amplitude. We focus on the position that significantly influences parameters including the area oscillation and obtain a better gap configuration to reduce the pressure fluctuation there. It is expected that the present results will contribute to the realization of a more reliable planetary landing system as a fundamental survey excluding the complex canopy deformation and the forebody interaction.

II. Numerical Setup

A. DGB Parachute Model Configuration

In the study, we use two types of rigid models that mimic the DGB parachute to investigate the effect of the opening area configurations on the drag and the surface pressure distributions. Case 1 (Fig. 1a) mimics the rigid model used in the wind-tunnel test. In the rigid-model wind-tunnel tests [22], it is necessary to support the band. Thus, case 1 also has eight band-support structures at 45 deg intervals. Thus, the gap of case 1 is separated and discretized by the structure. The thickness (2 mm) and the (rectangular) leading-edge configuration were decided according to manufacturing tolerances [22].

Next, case 2 (Fig. 1b) simulates a traditional and actual DGB parachute. However, in case 2, suspension lines between the disk and band are omitted because they are extremely thin (please see Refs. [6,10] for their influences). Thus, the gap in case 2 is continuous. This is the main difference between case 1 and case 2.

The Cartesian coordinate system (x, y, z) is defined such that its origin corresponds to the center of the leading edge of the parachutes. Specifically, the x axis is along the direction of the central axis of the parachute, the y axis is defined so that the angle of attack is defined around it, and the z axis is orthogonal to the aforementioned two.

The key geometric parameters of the two types of DGB parachutes are shown in the following (Table 2, and Figs. 1c and 1d). All parameters (with the exception of the vent and related parameters) are consistent with the experiment [22]. In parachute development, the nominal (reference) area S_0 or the x-directional projected parachute surface area S_p (including opening areas such as gaps and vents) is traditionally used to calculate the aerodynamic coefficients. The nominal (reference) diameter D_0, for instance, is given as follows:

$$D_0 = \sqrt{4S_0/\pi} \qquad (1)$$

In Table 2, all the key parameters normalized by D_0 or S_0 are shown in brackets.

Additionally, the geometric porosity λ_g is an important parameter for supersonic parachute development. Specifically, λ_g denotes the geometric opening area per total parachute surface area and is given as follows:

$$\lambda_g = \frac{S_{\text{opening}}}{S_0} = \frac{(S_G + S_v)}{S_0} \qquad (2)$$

Based on Table 2, the geometric porosity of case 1 $\lambda_{g,\text{case1}}$ is 8.2% and that of case 2 $\lambda_{g,\text{case2}}$ is 11.9%. For reference purposes, the geometric porosity of the Mars Science Laboratory is approximately 12.8% [23]. In terms of the geometric porosity, the parameter that is presently used is different because our DGB parachute configuration mimics a wind-tunnel experiment model as previously described. Thus, this is not a problem. Our motivation involves understanding basic flow physics by comparing computational results with the wind-tunnel experimental results.

B. Governing Equations

In the study, the governing equations are three-dimensional compressible Navier–Stokes equations as follows [Eqs. (3a–3c)]:

$$\frac{\partial \boldsymbol{Q}}{\partial t} + \frac{\partial \boldsymbol{Fe}_k}{\partial x_k} = \frac{1}{Re} \frac{\partial \boldsymbol{Fv}_k}{\partial x_k} \qquad (3a)$$

$$\boldsymbol{Q} = \begin{pmatrix} \rho \\ \rho u_l \\ e_T \end{pmatrix}, \qquad \boldsymbol{Fe} = \begin{pmatrix} \rho u_k \\ \rho u_l u_k + p\delta_{lk} \\ (e_T + p)u_k \end{pmatrix},$$

$$\boldsymbol{Fv} = \begin{pmatrix} 0 \\ \tau_{lk} \\ u_m \tau_{mk} + \dfrac{\kappa}{(\gamma - 1)\, Pr} \dfrac{\partial T}{\partial x_k} \end{pmatrix} \qquad (3b)$$

Table 2   Key geometric parameters of the DGB parachute

Parameter	Value
Nominal (reference) diameter D_0, mm	53.8
Projected diameter D_p, mm	40.0
$[D_p/D_0]$	[0.744]
Vent diameter D_v, mm	4.90
$[D_p/D_0]$	[0.091]
Band height, H_B (mm)	4.83
$[H_B/D_0]$	[0.090]
Gap height H_G mm	2.00
$[H_G/D_0]$	[0.037]
Canopy height H_C, mm	17.5
$[H_C/D_0]$	[0.325]
Nominal (reference) area S_0, mm^2	2.27×10^3
Projected area, S_p, mm^2	1.26×10^3
$[S_p/S_0]$	[0.553]
Gap areas $S_{G,\text{case1}}$ and $S_{G,\text{case2}}$, mm^2	1.67×10^2, 2.51×10^2
$[S_{G,\text{case1}}/S_0, S_{G,\text{case2}}/S_0]$	[0.074, 0.111]
Vent area S_v, mm^2	1.89×10^1
$[S_v/S_0]$	[0.0083]
Geometric porosities $\lambda_{g,\text{case1}}$ and $\lambda_{g,\text{case2}}$, %	8.2, 11.9

$$\tau_{jk} = \mu\left(\frac{\partial u_j}{\partial x_k} + \frac{\partial u_k}{\partial x_j}\right) - \frac{2}{3}\mu\frac{\partial u_l}{\partial x_l}\delta_{jk} \tag{3c}$$

where subscripts k, l, m, and n correspond to 1, 2, and 3 denoting the Cartesian coordinates; ρ denotes the density; u_i denotes the velocity components ($i = 1, 2$, and 3 corresponding to u, v, and w, respectively); e_T denotes the total energy per unit volume; p denotes the pressure; H denotes the total enthalpy [$H = (e_T + p)/\rho$]; and T denotes the temperature. The working gas is air, which is approximated by the calorically perfect gas model with the specific heat ratio of $\gamma = 1.4$. The Prandtl number is $Pr = 0.71$. The molecular viscosity μ as calculated via Sutherland's formula and thermal conductivity κ are related as $\kappa = c_p\mu/Pr$, where c_p denotes the specific heat at constant pressure. To incorporate the turbulence effects, the molecular viscosity μ is replaced by ($\mu + \mu_t$), where μ_t denotes the turbulence viscosity. Similarly, κ is replaced by ($\kappa + c_p\mu_t/Pr_t$), and Pr_t denotes the turbulent Prandtl number corresponding to 0.90.

The Reynolds number is defined in Eq. (4) as follows:

$$Re = \frac{\rho_\infty a_\infty L_\infty}{\mu_\infty} \tag{4}$$

where L_∞ is a unit length (1 m), and a_∞ denotes a freestream sound speed. Note that this Reynolds number appears as a result of normalization of the Navier–Stokes equations, whereas U_∞ (a freestream velocity) may be used as a reference velocity when it comes to the experimental flow conditions, for instance.

C. Computational Methods

We conduct three-dimensional numerical computation by using Fast aerodynamic routines (known as FaSTAR) [24] developed at the Japan Aerospace Exploration Agency (JAXA) as a high-speed flow solver for unstructured grids. The system of equations [Eq. (3)] is discretized via a cell-centered finite volume method. We use DDES [20] based on the Spalart–Allmaras one-equation model with no tripping term f_{t2} with rotation correction (SA-noft2-R) as the turbulence model. This corresponds to a Reynolds-averaged Navier–Stokes/large-eddy simulation hybrid model. In the model, a near-wall region is modeled via SA-noft2-R (RANS family model), and the other regions are modeled via LES. As a result, each computational case can be completed within a few weeks at JAXA's second-generation supercomputer system. A numerical flux for an inviscid term is calculated by an advection upstream splitting method (AUSM)-type scheme, namely, simple low-dissipation AUSM [25]. The Green–Gauss-based weighted least-squares method [26] is used for gradient reconstruction with a Venkatakrishnan slope limiter [27]. With respect to the time integration method, a lower–upper symmetric Gauss–Seidel scheme [28] is adopted with a second-order backward difference.

D. Computational Grids

We use HexaGrid [29] (which is an automatic meshing tool developed at JAXA) to generate the unstructured computational grids based primarily on hexahedral Cartesian grids (that are not axisymmetric and will play a role in breaking the flow symmetry). The computational grids for case 1 and case 2 are shown in Figs. 2a and 2b, respectively. The coordinate system is defined as mentioned earlier in this paper. As shown in Fig. 2c, the computational domain corresponds to a $35D_0 \times 35D_0$ cube that is filled with hexahedra, prisms, pyramids, and tetrahedra; and the origin of the coordinate system (i.e., the parachute nose) is set at $8.75D_0$ downstream from the inflow boundary. Furthermore, the number of cells is approximately 8.6×10^6 for each case. To resolve the boundary layer, the first cell height is defined to satisfy $y^+ < 1$. Furthermore, the confirmation of grid convergence will be described in Sec. III.B.

E. Computational Conditions

The computational conditions are selected to correspond to the wind-tunnel test [22] conditions in Table 3, such as the freestream

Mach number $M_\infty = 2.0$, Reynolds number Re_{D_p} (based on the diameter of the body), total pressure p_0, and local pressure p_∞:

$$Re_{D_p} = \frac{\rho_\infty U_\infty D_p}{\mu_\infty} \tag{5}$$

Additionally, the angle of attack throughout the study corresponds to 0 deg.

F. Aerodynamic Coefficients

We defined the axial force coefficient and the pressure coefficient C_p as follows:

$$C_D = \frac{F_x}{q_\infty S_0} \tag{6}$$

$$C_p = \frac{p - p_\infty}{q_\infty} \tag{7}$$

where F_x denotes the x component force; p denotes local pressure; and p_∞ and q_∞ denote freestream pressure and dynamic pressure, respectively.

G. Pressure Measurement Point Distribution

We set 20 pressure measurement points on the surface of the parachute models to investigate pressure fluctuations. As shown in Fig. 3, 10 points were set on the exterior of the parachute, and the other 10 points were set on the interior of the parachute. The aim of the setting involves comparing the amount of exterior pressure fluctuations of the parachute with those interior the parachute. As shown in Fig. 3, measurement points 1–5 are set at the positions where the distance from the center corresponds to 20, 40, 60, 80, and 92.5% of the radius. The points are labeled with a subscript of "in" or "out" that denotes the interior or exterior of the parachute, respectively. Additionally, the points are also labeled with a subscript of "0" or "22.5" that denotes the azimuthal angle φ (see Fig. 3) around the x axis (center axis of the parachute) to investigate the effect of the band-support structure on pressure fluctuations. The point sequence of 1_0–5_0 is set in the range of the azimuthal angle of the "gap influence region," and the point sequence of $1_{22.5}$–$5_{22.5}$ is set in the range of the azimuthal angle of the "no gap influence region." For example, the measurement point that is termed as 1_{out0} denotes that the point at which the distance from the center corresponds to 20% of the radius exterior, and its azimuthal angle $\varphi = 0$.

## III. Results and Discussions

A. Validation

First, we conduct computations for two different parachute configurations to validate our computational methods and setup. A configuration (case 1) corresponds to the comparison in terms of the exterior surface flowfield of the parachute. Another configuration (a cylindrical parachute without gaps) is in terms of the interior pressure fluctuation of the parachute.

#### 1. Surface Flowfield Validation for Unsteady Computations

To validate our unsteady computations, we compare a time-averaged solution of our unsteady computation with the final result of an oil flow experiment [22] that is assumed to capture a global and large-scale (low-frequency) surface flowfield. We create the averaged data by using 100 files with 500 time-step intervals (i.e., averaged over every 0.0935 s). Therefore, the total average section is 9.35 s. Figure 4 shows both computational and experimental exterior surface flowfields of the DGB parachute model. As shown in the figures, our computational result is in qualitative agreement with the experimental result [22] in terms of the following: 1) patterns of origin of longitudinal vortex V1, 2) patterns of the reattachment line of the horseshoe vortex, and 3) patterns of reverse flow.

We discuss the aforementioned three patterns. Initially, we focus on pattern 1. The patterns are generated at both ends of each single

a) Case 1 (perspective view)   b) Case 2 (perspective view)

8.75D_p 35D_p
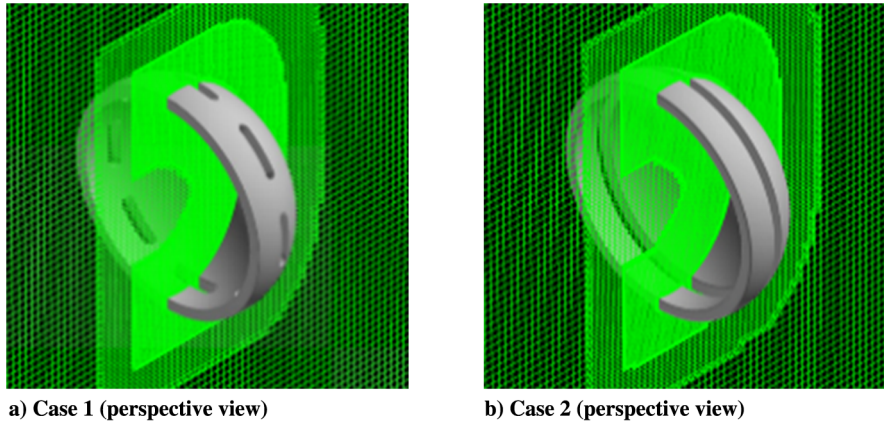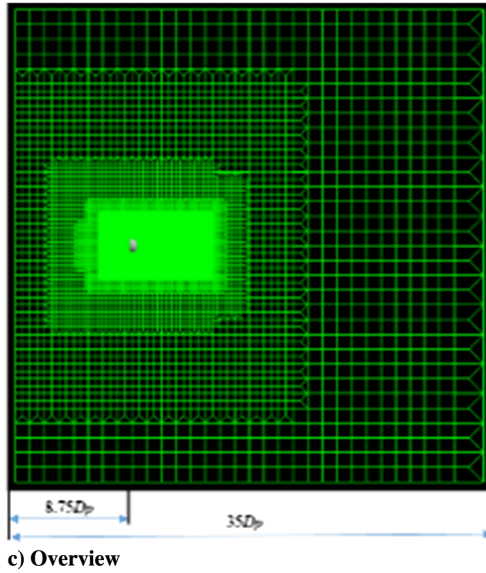
c) Overview

Fig. 2   Computational grid.

Table 3   Conditions of the supersonic wind-tunnel test (computation)

M_∞	2.0
Re_{Dp}	6.60×10^5
p_0, kPa	1.32×10^2
p_∞, kPa	1.71×10^1
T_∞, K	177.78

gap hole, and we considered this as generated by the longitudinal vortex V_L (see Fig. 5). Pattern 2 is termed as the reattachment line of the horseshoe vortex. Additionally, in the computational result, the line is closer to the gap hole than the experimental result. We assume that the difference is made by the turbulence model we used (SA-noft2-R-based DDES). In the model, regions near the wall are calculated by the SA-noft2-R RANS model. The model tends to overestimate the horseshoe vortex. In this case, a possibility exists wherein the primary vortex of the horseshoe vortex can be

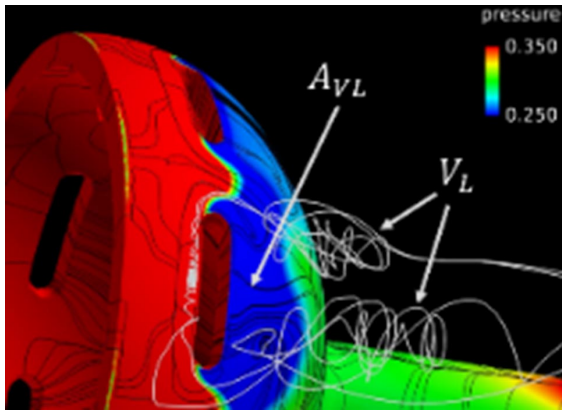**Fig. 3   Pressure measurement point distribution.**

a) Surface flowfield of the computation (case 1)

b) Surface flowfield of the oil flow experiment [22]

c) Initial condition of the oil flow experiment [22]
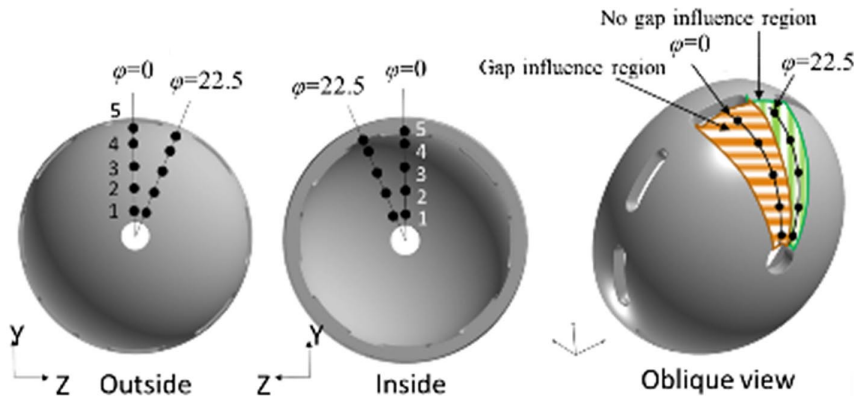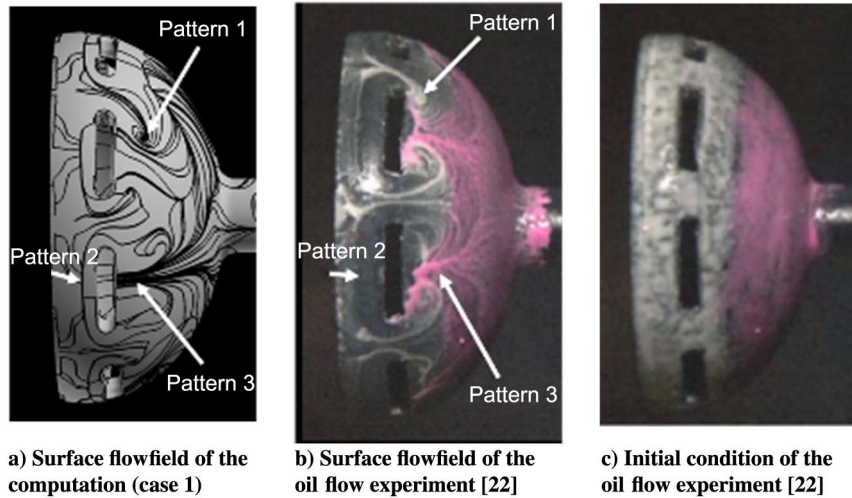
Fig. 4　Surface flowfield validation.

Fig. 5　Longitudinal vortex behind the gap (colored by static-pressure-normalized pressure p/p_∞ instead of C_p).

Fig. 6　Simplified cylindrical parachute model.

overestimated (a pure LES may improve this, but at an expense of tremendous cost, which is beyond the scope of the present work). Finally, the patterns of reverse flow (pattern 3) are observed in both results. In the experiment, the downstream-half part corresponding to the exterior of the model is colored by pink oil (see Fig. 4c). Therefore, the forward movement of pink oil in Fig. 4b represents the reverse flow.

2.　Pressure Fluctuation Validation for Unsteady Computations

To validate our unsteady computational method, we compare the pressure fluctuations in our unsteady computation result with the fluctuations in the wind-tunnel test result that used a more simplified, cylindrical parachute model (Fig. 6 [5]). The pressure measurement point is set at the position wherein the distance corresponds to half of the depth X_d of the model. The position of the pressure measurement point corresponds to that in the experiment [5]. Figure 7 shows the result of the comparison. The computational result (orange-colored dashed line) captures two characteristics of the experimental result. The first characteristic is that the experimental result corresponds to δp in the range of 100–400 Hz. The other characteristic is that it is constant in the ranges of 10–100 and 400–1000 Hz. Therefore, we observed that our computational method sufficiently captures the characteristics of pressure fluctuations in the range of 10–1000 Hz.

B.　Drag Coefficient Average and Fluctuations

1.　Unsteady Calculation and Average of Drag

An extremely important aspect of parachute performance is drag. Thus, we compare the drag coefficient C_D of case 1 with that of
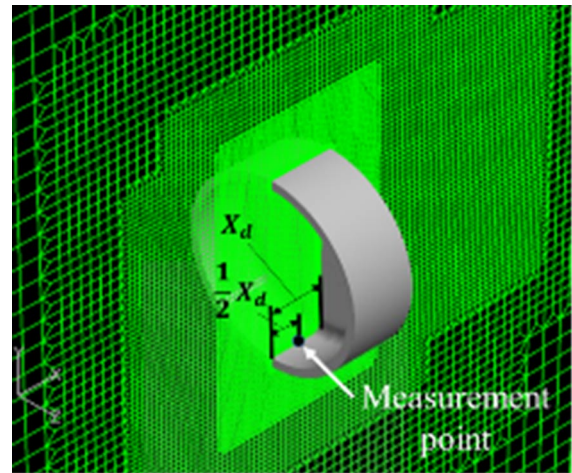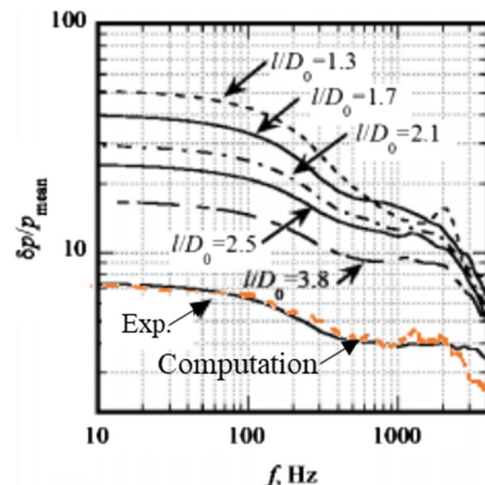

Fig. 7　Spectrums of interior pressure fluctuations of the parachute model [5].

case 2. The unsteady computation is conducted in two stages as shown in the following:

1) The first stage (preparation) has 30,000 time steps of unsteady calculation with $\Delta t = 7.5 \times 10^{-5}$ s [maximum Courant–Friedrichs–Lewy (CFL) $\approx$ 1900].

2) For the second stage (data acquisition), after the first-stage calculation, a 60,000-time-step unsteady calculation with $\Delta t = 7.5 \times 10^{-5}$ s (CFL $\approx$ 1900) is conducted.

To eliminate the effect of the initial condition and to obtain the original unsteadiness, the data obtained from second-stage calculation were adopted. In the range of time, initially, we compared the average of C_D ($C_{D,\text{ave}}$), as shown in Table 4. The average is conducted by using the second-stage data. Additionally, $C_{D,\text{ave}}$ in case 1 is 0.928, and case 2 is 0.918; i.e., the $C_{D,\text{ave}}$ in case 1 is 1.1% higher than that in case 2. These results are obtained by using a "medium" computational grid in which a grid convergence was confirmed [see Fig. 8]. The result shown in Fig. 8 indicate that the medium grid is enough to eliminate the influence of grid resolution on $C_{D,\text{ave}}$. Herein, the cell number N of each grid is shown in Table 5. For reference, there is the shape and the drag coefficients of another rigid DGB parachute model (having one-half of an ellipsoidal configuration, made of nylon, with the undisclosed geometric porosity λ_g) for another wind-tunnel test [30]. The $C_{D,\text{ave}}$ of this model is 0.88, and this value is very similar to those obtained in the present study. The slight discrepancies from case 1 or case 2 would have come from the differences in the curvatures of the disk region and the geometric porosity λ_g.

2. Fluctuation Amount of Drag

Second, we also calculate the standard deviation of the fluctuation of C_D (σ_{CD}) to quantitatively compare the fluctuation amount of the cases. As shown in Table 4, σ_{CD} of case 1 was 5.72×10^{-4}, and σ_{CD} of case 2 was 14.8×10^{-4}. Thus, the results indicate that the drag fluctuation amount of case 1 is approximately 60% smaller than that of case 2. In terms of the two indices, case 1 may be preferable as a decelerator for use at Mach 2 because it exhibits the characteristics of

Table 4 Average and standard deviations of the C_D fluctuation ($C_{D,\text{ave}}, \sigma_{\text{CD}}$)

	$C_{D,\text{ave}}$	σ_{CD}
Case 1	0.928	5.72×10^{-4}
Case 2	0.918	14.8×10^{-4}
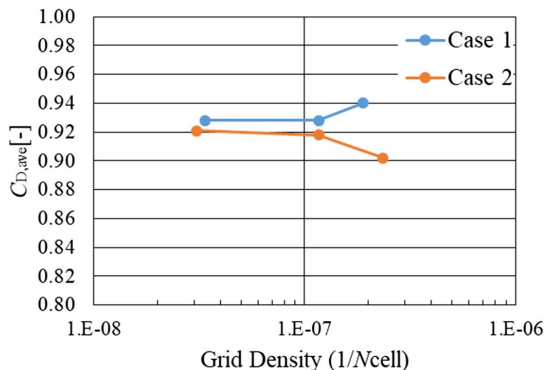
Fig. 8 Grid convergence confirmation.

Table 5 Cell number of each grid

	Case 1 {N cells (1/N)}	Case 2 {N cells (1/N)}
Coarse	$5.3 \times 10^6 (1.9 \times 10^{-7})$	$4.2 \times 10^6 (2.4 \times 10^{-7})$
Medium	$8.6 \times 10^6 (1.2 \times 10^{-7})$	$8.6 \times 10^6 (1.2 \times 10^{-7})$
Fine	$29.6 \times 10^6 (3.4 \times 10^{-8})$	$32.3 \times 10^6 (3.1 \times 10^{-7})$

high drag force and low drag fluctuation amount, although both of those fluctuations are very small compared with the average values.

3. Frequency Component of Drag Fluctuation

Third, in the range of time, we conduct a Fourier transform on the data of drag fluctuations to clarify major frequency components involved in the fluctuation. The results are shown in Fig. 9 as power spectral density (PSD) dual logarithmic graphs. In the graphs, the orange-colored curve shows the original data of the PSD. Furthermore, the blue-colored curve shows the simple moving average (SMA) of the original data to indicate the rough trends of original data. Subsequently, adjacent 20 data are used to conduct the SMA. Figure 9a shows the PSD of case 1. The results indicated that the PSD decreases almost quadratically until approximately 18 Hz, and thereafter decreases nearly linearly with respect to the frequency. Figure 9b shows the PSD of case 2. The characteristic of the graph is that the PSD in the range of 10–160 Hz is especially high when compared to that in case 1. The reason for this will be discussed in detail in Sec. III.E.

C. Surface Pressure Fluctuations for the Interior and Exterior

1. Exterior and Interior Surface Pressure Fluctuation Amounts

We focus on the surface pressure fluctuations interior and exterior each case. A surface pressure fluctuation is important because it involves deformation of the parachutes. We focus on 20 pressure measurement points, and their distributions are shown in Fig. 3. Based on the data obtained from the points, we calculate the standard deviation of the pressure fluctuation to evaluate the amount of fluctuations quantitatively. Table 6 shows the average of standard deviations of pressure fluctuations $\sigma_{p,\text{ave}}$. As shown in the table, in case 1, the $\sigma_{p,\text{ave}}$ exterior is approximately five times that on the interior. Therefore, the outer pressure fluctuation is dominant in case 1. Conversely, in case 2, the $\sigma_{p,\text{ave}}$ exterior is only 1.2 times that on the interior. Therefore, the results indicate that the interior pressure fluctuation is significant when compared with that in case 1. Specifically, the pressure fluctuation of interior case 2 is 9.6 times that in case 1. Furthermore, the pressure fluctuation of exterior case 2 is approximately 2.3 times that of case 1. (Thus, in case 2, the gap configuration has reduced the interior pressure fluctuation by approximately 90% and the exterior pressure fluctuation by 57%.) Based on the results, pressure and drag fluctuations are significantly underestimated while using the gap shape (case 1) that is tested on the wind tunnel.

2. σ_p of Each Pressure Measurement Point

The next topic corresponds to the σ_p of each pressure measurement point. Figures 10a and 10b show the σ_p on the exterior and interior, respectively, in case 1. Figures 10c and 10d show the σ_p on the exterior and interior, respectively, in case 2. As shown in Fig. 10a, while the σ_p of measurement point 1 is highest at $\phi = 0$ (1_{out0}), the σ_p of measurement point 3 is highest at $\varphi = 22.5$ ($3_{\text{out22.5}}$). As shown in the result, the σ_p on exterior case 1 exhibits a phase difference due to the influence of the discretized gap. The mechanism of the large fluctuation on the $3_{\text{out22.5}}$ is explained later in Sec. III.E. Conversely, as shown in Fig. 10c, the σ_p of measurement point 2 is highest at each azimuthal angle φ (2_{out0}, $2_{\text{out22.5}}$). The mechanism of the large fluctuation on 2_{out0} is also explained later in Sec. III.E. As shown in the figure, the magnitude of the σ_p varies only based on the radial distance, and its magnitude correlation is the same in each azimuthal angle φ because of the absence of the model shape difference between the azimuthal angles of 0 and 22.5. As shown in Fig. 10d, the σ_p of measurement point 4 is the highest at each azimuthal angle φ; similarly, the magnitude correlation of σ_p is the same in each azimuthal angle φ.

Conversely, it is known that an area oscillation (which corresponds to a problematic instability phenomenon of a supersonic parachute) occurs when the region far from the center is deformed [6]. Therefore, in order to suppress the area oscillation, it is considered as effective to reduce the pressure fluctuation in the region far from the center, such as measurement points 4 and 5 in the study. Figure 10e shows
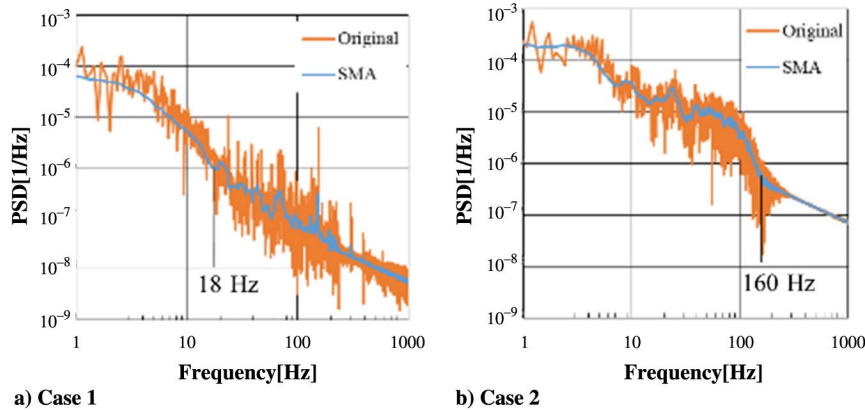
a) Case 1   b) Case 2

Fig. 9   PSD graphs of C_D fluctuations.

Table 6   Average of the standard deviations of the pressure fluctuation ($\sigma_{p,\text{ave}}$)

	Exterior	Interior
Case 1	5.83×10^{-3}	1.19×10^{-3}
Case 2	13.6×10^{-3}	11.5×10^{-3}

the result of extracting σ_p of measurement points 4 and 5 in each case. A comparison with case 2 indicates that the decrease in σ_p interior case 1 is significant. The concrete mechanism for this will be explained subsequently in Sec. III.E. Furthermore, the sum of the σ_p of measurement points 4 (interior and exterior) and 5 (interior and exterior) in case 1 is reduced by approximately 70% when compared to that in case 2 (see Fig. 10f). Therefore, case 1 (which exhibits a more complex configuration) appears to be better in terms of area oscillation suppression. On the actual, flexible parachute surface, the interior and the exterior pressures mutually interact and different modes might be activated. In such a case, the location of the pressure maximum might be different, and a parametric study taking the model structure into account will be necessary for stability analysis. But, still, the present findings will be useful pieces of information for fundamental understanding of the unsteady pressure fluctuations and their effects on the parachute deformation. Moreover, the present results directly apply to the early stages of the parachute development in which a rigid model is widely used.

D.   Relation Between Surface Pressure Fluctuations and Drag Coefficient Fluctuations

In the previous section, we discussed the surface pressure fluctuations and drag coefficient fluctuations. In this section, we consider the part of the parachute that significantly contributes to the drag fluctuations by surveying the frequency component of each fluctuation.

1.   Case 1

First, we focus on case 1, which exhibits a large pressure fluctuation on the exterior as mentioned in the previous section. As shown in Fig. 11a, the power spectral density graph of the drag fluctuation of case 1 superimposed on the PSD graphs of pressure measurement points $1_{\text{out22.5}}$ and $3_{\text{out22.5}}$. The points are selected because they exhibit the highest and second highest σ_p, and they adequately represent the frequency characteristics of the fluctuations in the surrounding points (see Figs. 11c and 11d). For example, in Fig. 11c, four PSD graphs of measurement points including $3_{\text{out22.5}}$ are shown. These are located near the $3_{\text{out22.5}}$, and these PSD graphs show almost identical trends. This indicates that these PSD graphs have different values but have similar frequency characteristics. Therefore, the frequency characteristics of $3_{\text{out22.5}}$ represent its surrounding points, and they can attribute to the frequency characteristics of drag less than 15 Hz. As seen in Fig. 11a, for 15 Hz or less, the PSD of $3_{\text{out22.5}}$ exhibits good agreement

with the PSD of C_D. With respect to the PSD of $1_{\text{out22.5}}$, on the other hand, it exhibits good agreement with the PSD of C_D in the range of more than 15 Hz. Thus, the drag fluctuation of less than 15 Hz is attributable to the position of $3_{\text{out22.5}}$, and the fluctuation exceeding 30 Hz is attributable to $1_{\text{out22.5}}$.

2.   Case 2

Next, let us focus on case 2. As mentioned in the previous section, it is necessary to consider the interior and exterior pressure fluctuations. As shown in Fig. 11b, the PSD graph of the drag fluctuation in case 2 overlaps with the PSD graphs of pressure measurement points 2_{out0} and 4_{in0}. The PSDs of 2_{out0} and 4_{in0} are selected because they exhibit the highest σ_p on the exterior and interior, respectively, and adequately represent the frequency characteristics of the fluctuation in the surrounding points (see Figs. 11e and 11f). Figure 11e indicates that these PSD graphs excluding 2_{out0} show good agreement for 2_{out0} of less than 20 Hz. Therefore, 2_{out0} can attribute the frequency characteristics of drag of less than 9 Hz. In addition, Fig. 11f shows that these PSD graphs excluding 4_{in0} exhibit good agreement for 4_{in0} in the range of 20–200 Hz. As shown in Fig. 11b, the results indicate that the PSD of 2_{out0} is consistent with the PSD of C_D in the range of less than 9 Hz. It was also observed that the PSD of 4_{in0} exhibits good agreement with the PSD of C_D in the range exceeding 100 Hz. The agreements suggest that the drag fluctuation of less than 9 Hz mainly occurs at the position corresponding to 2_{out0} and the fluctuation of more than 100 Hz is attributable to 4_{in0}.

As shown in the results for case 1 and case 2, the positions that significantly contribute to the drag fluctuation are identified. It is considered that the aforementioned positions would contribute to the future improvement of a conventional DGB parachute, at least for the present setup. Additionally, in each case, the results indicate that the C_D fluctuation of the entire parachute can be represented by the PSD graph at only two points on its surface. These remarks will be verified by taking the forebody and the model support into account in future work.

E.   Relationship Between the PSD Graph and Flowfield

In the previous section, we clarified the relationship between the fluctuation components of the pressure fluctuation and the position. In this section, we discuss how the pressure fluctuations are created by the flowfield.

1.   Case 1: Exterior

Initially, we focus on case 1. Figure 12 shows a period of variation in the pressure distribution of the $3_{\text{out22.5}}$ in case 1. The black lines on the surface of the parachute denote the surface streamline. As shown in Fig. 12, there are approximately four regions termed as area of the longitudinal vortex A_{VL}. A_{VL} is generated by longitudinal vortices and barely moves. Therefore, the main pressure fluctuation by moving of the reattachment region occurs in the region, with the exception of A_{VL}
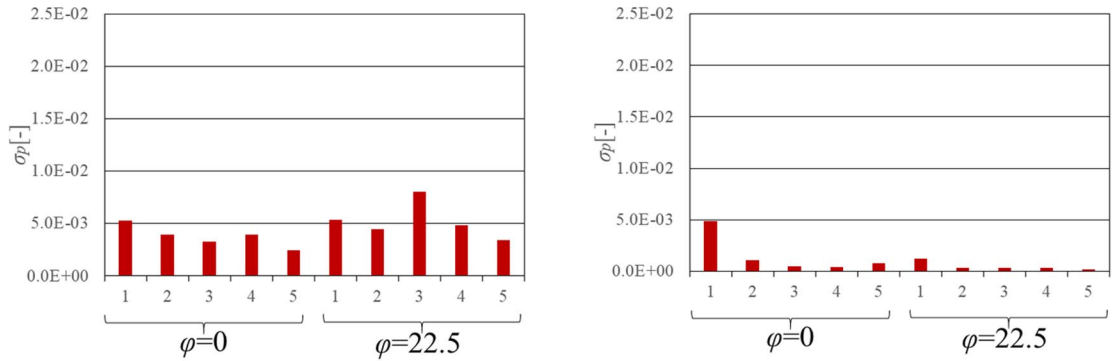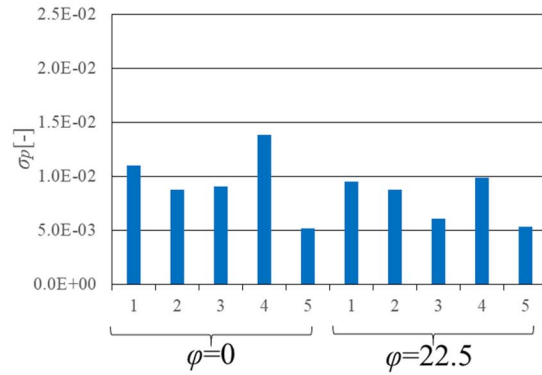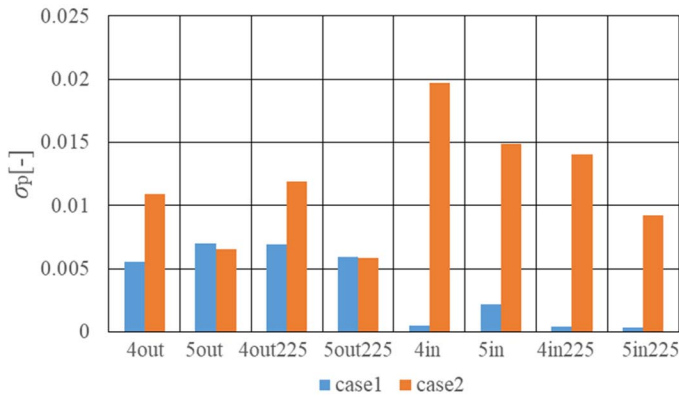
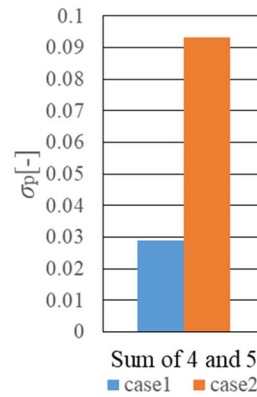a) Case 1: exterior

b) Case 1: interior
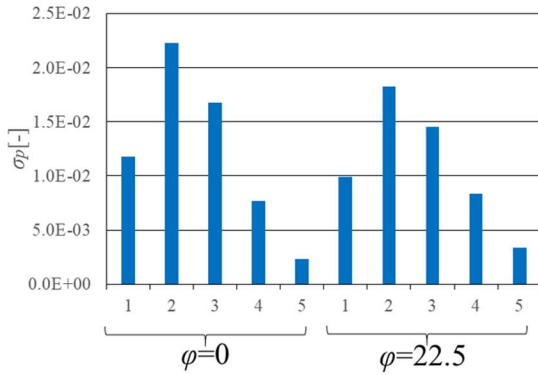
c) Case 2: exterior

d) Case 2: interior

e) σ_p of measurement points 4 and 5

f) Sum of the σ_p of measurement points 4 (interior and exterior) and 5 (interior and exterior)

Fig. 10 σ_p of each pressure measurement point.

(the schematic is shown in Fig. 13). The period of visualization T in the figure is approximately 0.15 s ($\cong$7 Hz). We defined the time instant in Fig. 12a as $t/T = 0.0$, and the results indicate that the pressure of $3_{out22.5}$ increases until $t/T = 0.5$ because the reattachment region R that indicates relatively high pressure gradually covers $3_{out22.5}$. Subsequently, the pressure of $3_{out22.5}$ decreases until $t/T = 1.0$. As shown in case 1's interior, the σ_p of $1_{out22.5}$ is the highest, although the details of the flowfield at this point are omitted because the fluctuation near the center of the parachute is not expected to play a role in the area oscillations.

2. Case 2: Exterior

Next, we focused on the exterior of case 2. Figure 14 shows a period of variation in the pressure distribution of 2_{out0} in case 2. The period of visualization T in the figure is approximately 0.15 s ($\cong$ 7 Hz). We defined the time in Fig. 14a as $t/T = 0.0$ when the

low-pressure region due to separation S_R covers 2_{out0}. The results indicate that the pressure of 2_{out0} increases until $t/T = 0.5$ because relatively high-pressure region R approaches to 2_{out0}. Subsequently, given the approach of S_R, the pressure of 2_{out0} decreases again. In contrast to case 1, the reattachment region R and separated region S_R move in the whole exterior region of case 2 (the schematic is shown in Fig. 15). This leads to the difference in the pressure and drag fluctuation amount between case 1 and case 2. Additionally, Fig. 14 also shows the asymmetric pressure distribution of case 2's exterior. A band-support structure is absent in case 2, and thus A_{VL} that restricts the movement of R in case 1 is not formed. Therefore, the results indicate that the reattachment region R can be gathered to the left side in this figure. In the case of a flexible parachute, this could potentially cause one-half of a canopy to deform if the pressure at both sides mutually interacts significantly. Figure 16a shows the u velocity contours and velocity vectors of the flowfield near

a) Case 1

b) Case 2

c) Case 1: PSD graph near $3_{out22.5}$

d) Case 1: PSD near $1_{out22.5}$

e) Case 2: PSD graph near $2_{out 0}$
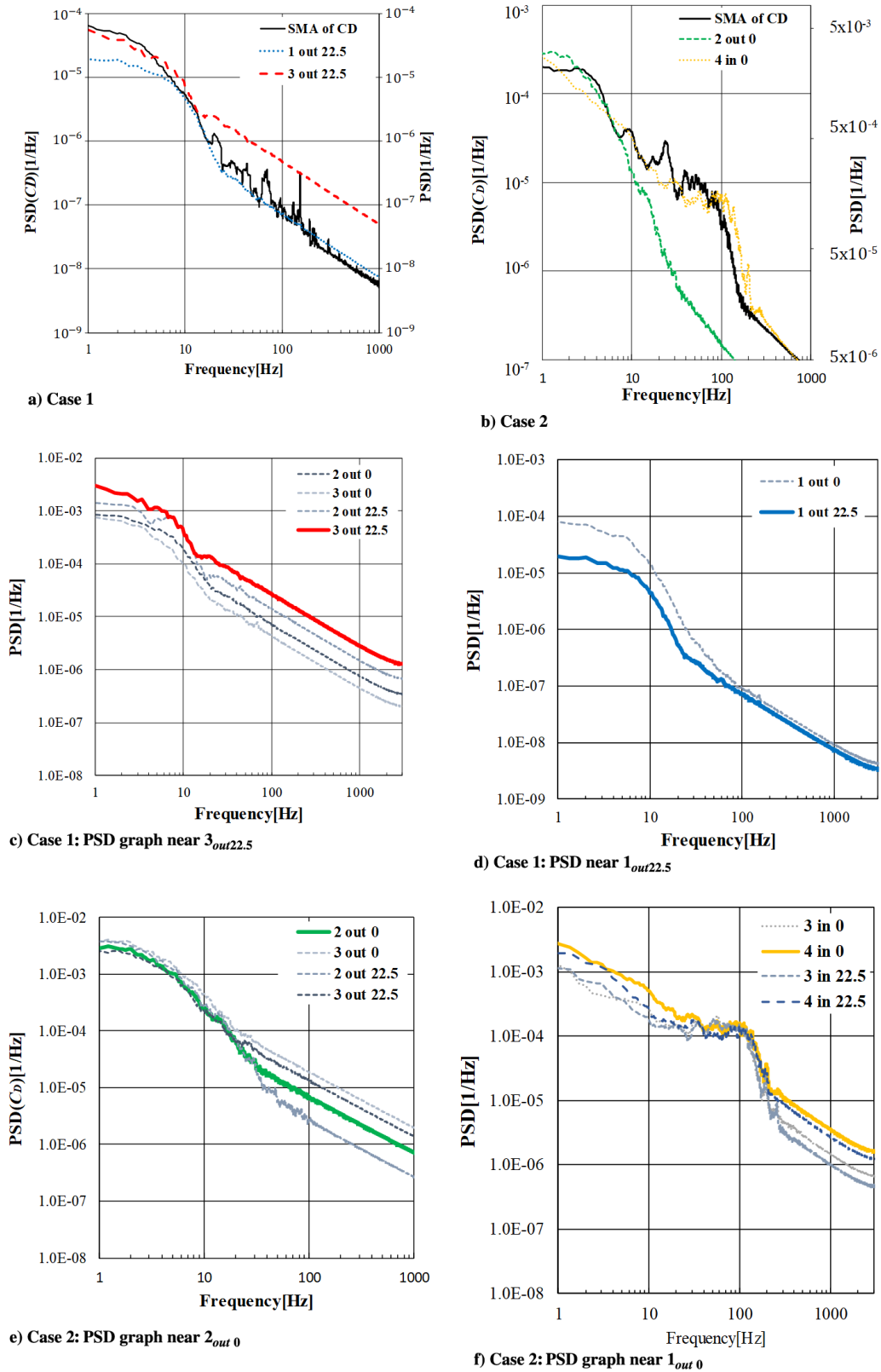
f) Case 2: PSD graph near $1_{out 0}$

Fig. 11   Relation between surface pressure and drag coefficient (C_D) fluctuation.

the reattachment region R at $t/T = 0.0$ in case 1 [this plane is $y/(D_p/2) = 0.55$]. The region colored in red represents the reverse flow region, and the reverse flow goes to reattachment region R. Similarly, Fig. 16b shows the u velocity contours and velocity vectors of the flowfield around R at $t/T = 1.0$ in case 2. As shown in the figure, it is observed that the reverse flow goes toward R. On the other

side of R (right side in this figure), separation and vortex regions are observed.

3.   *Case 2: Interior*

Finally, we focus on the interior of case 2. Figure 17 shows a single period of variation in the pressure distribution of 4_{in0} in case 2.

a) t/T = 0.0

b) t/T = 0.25

c) t/T = 0.5

d) t/T = 0.75

e) t/T = 1.0
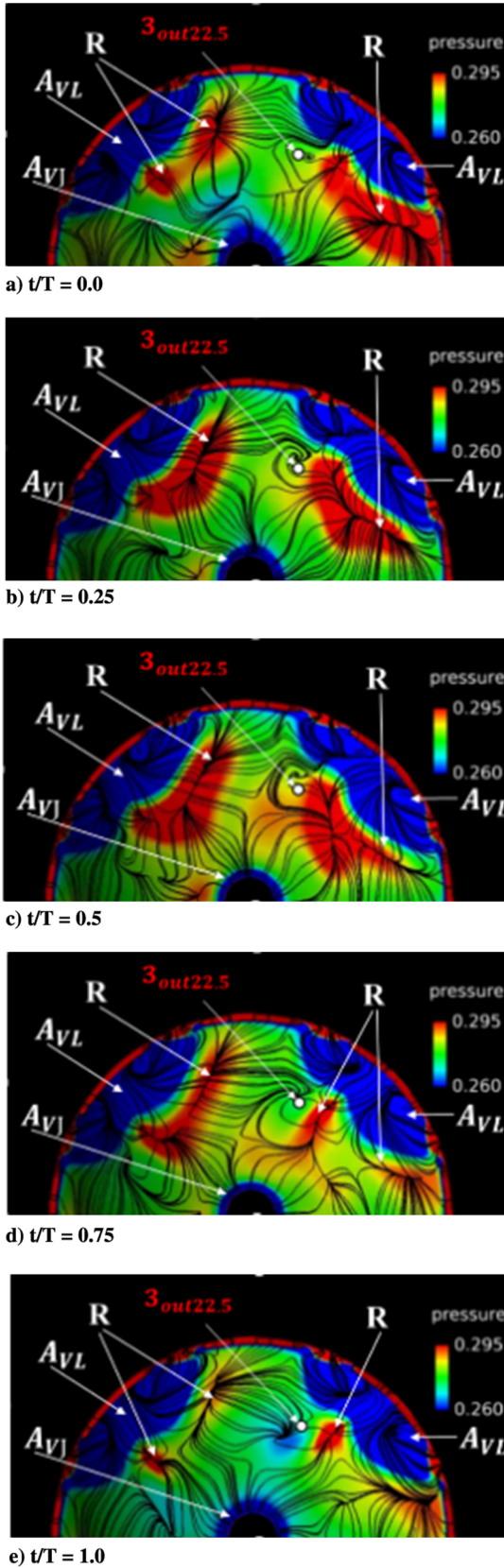
Fig. 12   Pressure (normalized by the freestream value) distribution variation in case 1.
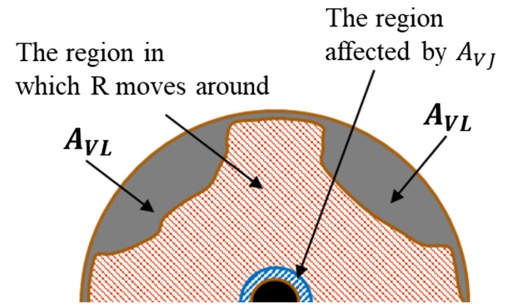

Fig. 13   Schematic of the area in which R moves around (case 1).

stagnation regions (S_t) gather to the lower-half in Fig. 17a, and the upper-half (left-half in Fig. 18a) corresponds to the vortex region. The pressure of 4_{in0} decreases until $t/T = 0.5$ when the expansion flow ("Exp.") becomes stronger (see Fig. 18b). Subsequently, the pressure of 4_{in} increases along with that of the complete region interior of the canopy. It was considered that the increase was caused by the departure of the vortex region from the interior wall of the canopy (see Fig. 18c). As shown in the result, in case 2, its pressure distribution exhibits large asymmetry even interior, and this causes large canopy deformation and collapse similar to that of the exterior. In contrast, when a band-support structure exists, this could act as a type of rectifying plate and can create a slightly symmetrical flow and pressure distribution interior of the canopy.

IV.   Conclusions

In the study, the CFD calculations were conducted to investigate the basic flowfield of the supersonic parachute (DGB type) and the two configurations were compared, wherein a configuration mimicked the wind-tunnel test model that exhibits a discrete gap opening area (case 1), and the other configuration mimicked a simplified actual configuration that exhibits a continuous gap opening area (case 2). Then, the following conclusions were obtained:

1) In terms of the amount of C_D fluctuation, the results indicated that case 1 exhibited 60% less C_D fluctuation than that in case 2. The result suggested that the drag fluctuation can be underestimated by using a general wind-tunnel test model.

2) In terms of the pressure fluctuation amount, in case 1, the fluctuation amount of the exterior was five times that of the interior. Thus, the fluctuation in the exterior was dominant because all of the fluctuation was generated by the interaction between jets from the gap or the vent and wake of the canopy. Additionally, the results indicated that the interaction generated the reattachment region on the exterior surface and the moving of the region caused the main drag fluctuation.

3) Conversely, in case 2, the fluctuation amount of the exterior was only 1.2 times that of the interior. This was because the interior also exhibits large asymmetry pressure distribution due to the lack of band-support structure. A comparison with the pressure distribution in case 1 indicated that the structure suppressed the exterior pressure fluctuation. The structure generated a vortex region that caused a relatively small pressure fluctuation backward and restricted the movement of the reattachment region, causing a high-pressure fluctuation. Without the structure, the amount of outflow from gap in each direction was gathered to a side, and its asymmetry produced large fluctuations. As described earlier in this paper, in case 2, large fluctuations occurred both interior and exterior, given that the benefit of the structure was absent.

4) From the area oscillation suppression viewpoint, case 1 was considered as a better configuration. This was because the area oscillation occurred when the position far from the parachute center was deformed; and the effect of the band-support structure, as previously described, reduced 70% of the pressure fluctuation.

5) In case 1, as shown in the PSD graph and visualization of the pressure distribution, the fluctuation of less than 15 Hz was considered to mainly occur at the position corresponding to approximately 60% of the radius from the center of the parachute. Additionally, the
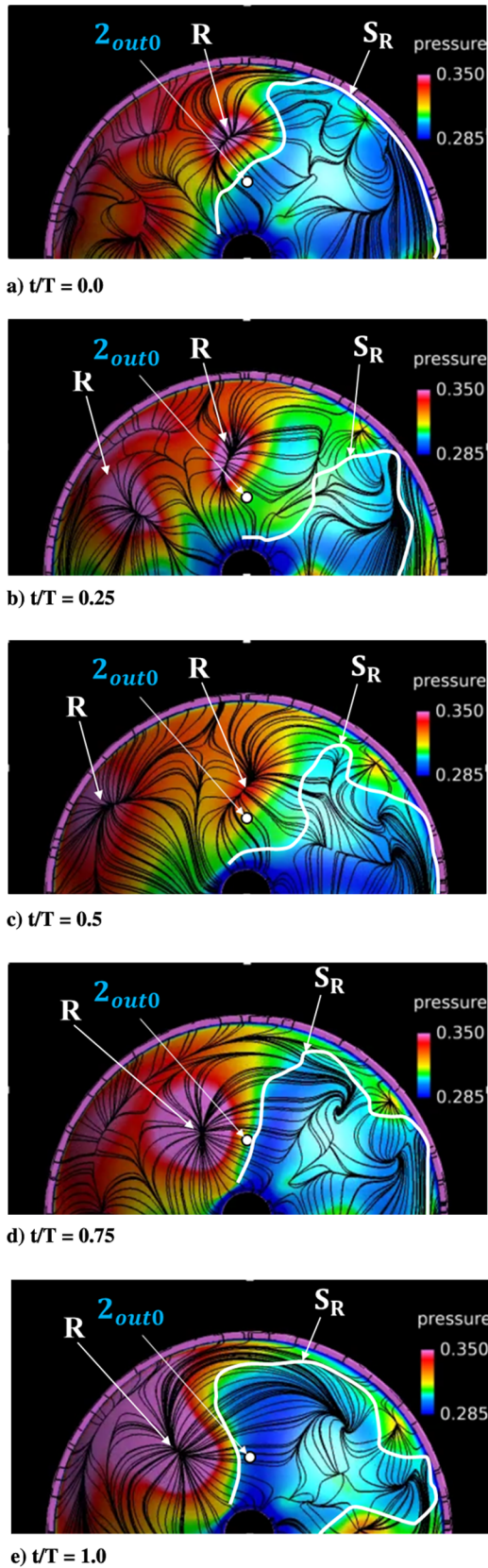
The period of visualization T in the figure is approximately 0.04 s (25 Hz), and we defined the time in Fig. 17a as $t/T = 0.0$ s. Figure 18 shows the contours of the pressure and y directional (see Fig. 3) velocity v vectors at $t/T = 0.0$, 0.5, and 1.0. When $t/T = 0.0$, the

a) t/T = 0.0

b) t/T = 0.25

c) t/T = 0.5

d) t/T = 0.75

e) t/T = 1.0

Fig. 14   Pressure (normalized by the freestream value) distribution variation in case 2.

fluctuation exceeding 15 Hz was considered to mainly occur at the exterior near the vent.

6) Similarly, in case 2, the fluctuation of less than 9 Hz was considered to mainly occur at the position corresponding to approximately 40% of the radius from the center of the parachute. In
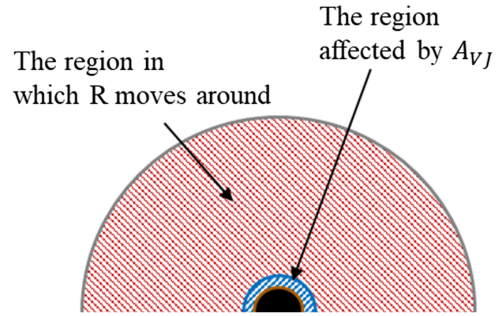

Fig. 15   Schematic of the area in which R moves around (case 2).

contrast, the fluctuation in the range of 100–200 Hz was considered to mainly occur at the position corresponding to approximately 80% of the radius from the center of the parachute.

The present, fundamental work has been limited to the rigid, impermeable assumption on the canopy with a relatively large thickness, as well as the absence of the forebody or suspension lines, while geometrical porosities of the gap and vent have been considered. These will be taken into account in future studies for better explanations on the wake flows, their interaction with the canopy deformation, and the other detailed parts at higher frequencies. A higher Mach number or Reynolds number (i.e., larger geometries) will also provoke higher-frequency modes, calling for extra computational burdens; such a survey is also currently planned as a separate work, as well as a survey on the support effect in the wind-tunnel experiment. Taking all these into account will eventually lead to a good guideline for designing
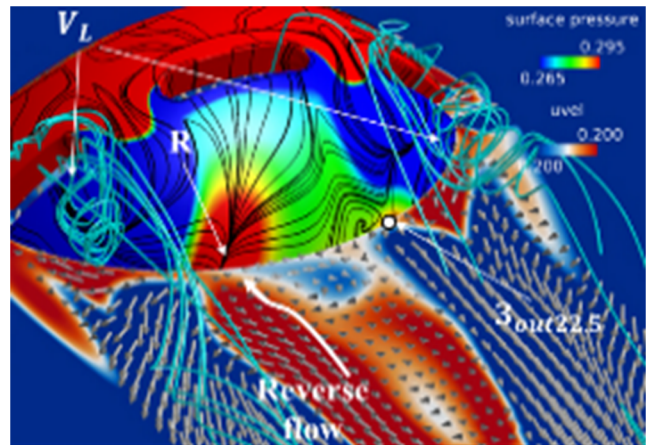
a) Case 1
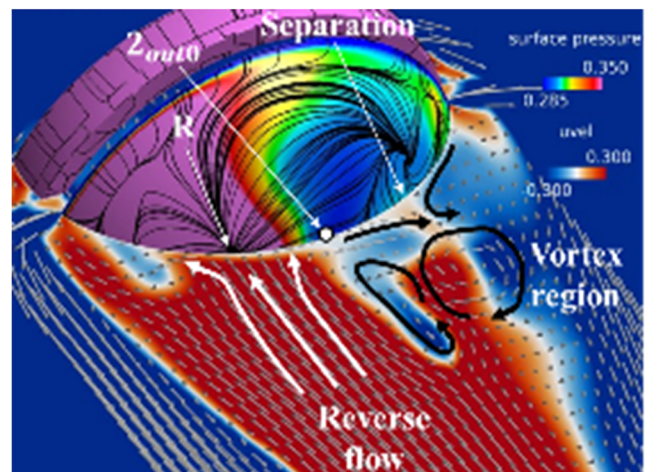
b) Case 2

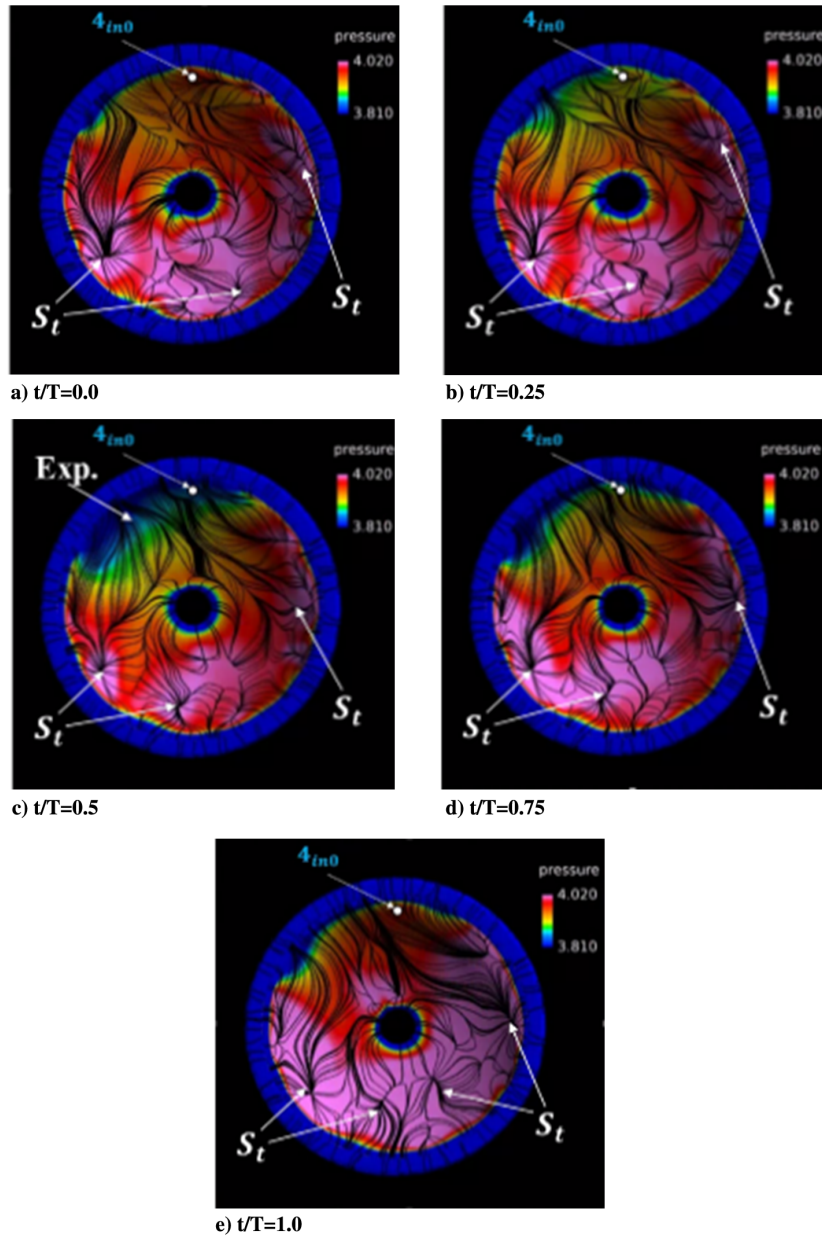**Fig. 16   Reattachment region and surrounding flow.**

a) t/T=0.0

b) t/T=0.25

c) t/T=0.5

d) t/T=0.75

e) t/T=1.0

Fig. 17   Pressure (normalized by the freestream value) distribution variation for case 2 (interior).
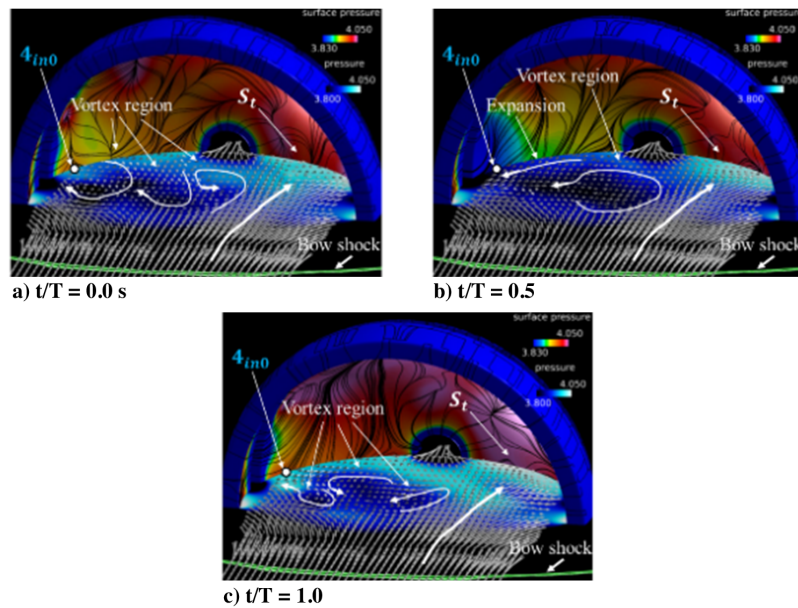
a) t/T = 0.0 s

b) t/T = 0.5

c) t/T = 1.0

Fig. 18   Pressure (normalized by the freestream value) fluctuation and flowfield interior the canopy in case 2.

novel parachute configurations and further developments of the related studies.

Acknowledgments

References

[1] Cruz, J. R., and Lingard, J. S., "Aerodynamic Decelerators for Planetary Exploration: Past, Present, and Future," *AIAA Guidance, Navigation, and Control Conference and Exhibit*, AIAA Paper 2006-6792, 2006. https://doi.org/10.2514/6.2006-6792

[2] Maydew, R. C., Peterson, C. W., and Orlik-Ruckemann, K. J., "Design and Testing of High-Performance Parachutes," AGARDograph 319, Neuilly-Sur-Seine, France, 1991, p. 12, https://www.sto.nato.int/publications/AGARD/AGARD-AG-319/AGARD-AG-319.pdf [retrieved 29 July 2020].

[3] Reichenau, D. E., "Aerodynamic Characteristics of Disk-Gap-Band Parachutes in the Wake of Viking Entry Forebodies at Mach Numbers from 0.2 to 2.6," Arnold Engineering Development Center AEDC-TR-72-78, Arnold AFB, TN, 1972, https://apps.dtic.mil/dtic/tr/fulltext/u2/746291.pdf [retrieved 29 July 2020].

[4] Sengupta, A., Steltzner, A., Witkowski, A., Candler, G., and Pantano, C., "Findings from the Supersonic Qualification Program of the Mars Science Laboratory Parachute System," *AIAA Aerodynamic Decelerator Systems Conference*, AIAA Paper 2009-2900, 2009. https://doi.org/10.2514/6.2009-2900

[5] Semba, N., Kuzuo, K., Taguchi, M., and Mori, K., "Statistical Characteristics of the Pressure Oscillation in the Canopy of Supersonic Parachute," *Journal of the Society for Aeronautical and Space Sciences*, Vol. 65, No. 2, 2017, pp. 64–72 (in Japanese).

[6] Karagiozis, K., Kamakoti, R., Cirak, F., and Pantano, C., "A Computational Study of Supersonic Disk-Gap-Band Parachutes Using Large-Eddy Simulation Coupled to a Structural Membrane," *Journal of Fluids and Structures*, Vol. 27, No. 2, 2011, pp. 175–192. https://doi.org/10.1016/j.jfluidstructs.2010.11.007

[7] Sengupta, A., Roeder, J., Kelsch, R., Wernet, M., Kandis, M., and Witkowski, A., "Supersonic Disk Gap Band Parachute Performance in the Wake of a Viking-Type Aeroshell from Mach 2 to 2.5," AIAA Paper 2008-6217, 2008. https://doi.org/10.2514/6.2008-6217

[8] Kim, Y., and Peskin, C. S., "3-D Parachute Simulation by the Immersed Boundary Method," *Computers and Fluids*, Vol. 38, No. 6, 2009, pp. 1080–1090. https://doi.org/10.1016/j.compfluid.2008.11.002

[9] Xue, X., and Nakamura, Y., "Numerical Simulation of a Three-Dimensional Flexible Parachute System Under Supersonic Conditions," *Transactions of the Japan Society for Aeronautical and Space Sciences, Aerospace Technology Japan*, Vol. 11, Nov. 2013, pp. 99–108. https://doi.org/10.2322/tastj.11.99

[10] Xue, X., Koyama, H., Nakamura, Y., and Wen, C.-Y., "Effects of Suspension Line on Flow Field Around a Supersonic Parachute," *Aerospace Science and Technology*, Vol. 43, June 2015, pp. 63–70. https://doi.org/10.1016/j.ast.2015.02.014

[11] Xue, X.-P., Nishiyama, Y., Nakamura, Y., Mori, K., and Wen, C.-Y., "Parametric Study on Aerodynamic Interaction of Supersonic Parachute System," *AIAA Journal*, Vol. 53, No. 9, 2015, pp. 2796–2801. https://doi.org/10.2514/1.J053824

[12] Guruswamy, G. P., "Time-Accurate Coupling of Three-Degree-of-Freedom Parachute System with Navier–Stokes Equations," *Journal of Spacecraft and Rockets*, Vol. 54, No. 6, 2017, pp. 1278–1283. https://doi.org/10.2514/1.A33835

[13] Tezduyar, T. E., Takizawa, K., Moorman, C., Wright, S., and Christopher, J., "Space–Time Finite Element Computation of Complex Fluid–Structure Interactions," *International Journal for Numerical Methods in Fluids*, Vol. 64, Nos. 10–12, 2010, pp. 1201–1218. https://doi.org/10.1002/fld.2221

[14] Stein, K., Benney, R., Kalro, V., Tezduyar, T. E., Leonard, J., and Accorsi, M., "Parachute Fluid-Structure Interactions: 3-D Computation," *Computer Methods in Applied Mechanics and Engineering*, Vol. 190, Nos. 3–4, 2000, pp. 383–386. https://doi.org/10.1016/S0045-7825(00)00208-5

[15] "Performance of and Design Criteria for Deployable Aerodynamic Decelerators," U.S. Air Force ASD-TR-61-579, Dec. 1963, https://apps.dtic.mil/dtic/tr/fulltext/u2/429971.pdf [retrieved 29 July 2020].

[16] Heinrich, H. G., Ballinger, J. G., and Ryan, P. E., "Pressure Distribution in Transonic Flow of Ribbon and Guide Surface Parachute Models," U.S. Air Force WADC 59-32, Feb. 1959. https://apps.dtic.mil/dtic/tr/fulltext/u2/210257.pdf [retrieved 29 July 2020].

[17] Fric, T. F., and Roshko, A., "Vortical Structure in the Wake of a Transverse Jet," *Journal of Fluid Mechanics*, Vol. 279, Nov. 1994, pp. 1–47. https://doi.org/10.1017/S0022112094003800

[18] Aswin, G., and Chakraborty, D., "Numerical Simulation of Transverse Side Jet Interaction with Supersonic Free Stream," *Aerospace Science and Technology*, Vol. 14, No. 5, 2010, pp. 295–301. https://doi.org/10.1016/j.ast.2010.02.001

[19] Takayanagi, H., Suzuki, T., Yamada, K., Maru, Y., Matsuyama, S., and Fujita, K., "Development of Supersonic Parachute for Japanese Mars Rover Mission," *Transactions of the Japan Society for Aeronautical and Space Sciences, Aerospace Technology Japan*, Vol. 14, No. ists30, 2016, pp. Pe_87–Pe_94. https://doi.org/10.2322/tastj.14.Pe_87

[20] Spalart, P. R., Deck, S., Shuur, M. I., Squires, K. D., Strelets, M. K., and Travin, A., "A New Version of Detached–Eddy Simulation, Resistant to Ambiguous Grid Densities," *Theoretical and Computational Fluid Dynamics*, Vol. 20, No. 3, 2006, pp. 181–195. https://doi.org/10.1007/s00162-006-0015-0

[21] Pain, R., Weiss, P.-E., and Deck, S., "Zonal Detached Eddy Simulation of the Flow Around a Simplified Launcher Afterbody," *AIAA Journal*, Vol. 52, No. 9, 2014, pp. 1967–1979. https://doi.org/10.2514/1.J052743

[22] Kuzuo, K., Taguchi, M., Kurata, R., Arihama, K., and Mori, K., "Shape Effect on the Aerodynamics of Supersonic Parachute," *Transactions of the Japan Society for Aeronautical and Space Sciences* (in preparation).

[23] Cruz, J. R., Way, D., Shidner, J., Davis, J. L., Powell, R. W., Kipp, D., Adams, D. S., Sengupta, A., Witowski, A., and Kandis, M., "Parachute Models Used in the Mars Science Laboratory Entry, Descent, and Landing Simulation," *AIAA Aerodynamic Decelerator Systems Technology Conference*, AIAA Paper 2013-1276, 2013. https://doi.org/10.2514/6.2013-1276

[24] Hashimoto, A., Murakami, K., Aoyama, T., Hishida, M., Paulus, R. L., Sakashita, M., and Sato, Y., "Development of Fast Flow Solver FaSTAR," *Journal of the Society for Aeronautical and Space Sciences*, Vol. 63, No. 3, 2015, pp. 96–105 (in Japanese). https://doi.org/10.2322/jjsass.63.96

[25] Shima, E., and Kitamura, K., "Parameter-Free Simple Low-Dissipation AUSM-Family Scheme for All Speeds," *AIAA Journal*, Vol. 49, No. 8, 2011, pp. 1693–1709. https://doi.org/10.2514/1.J050905

[26] Shima, E., Kitamura, K., and Haga, T., "Green–Gauss/Weighted-Least-Squares Hybrid Gradient Reconstruction for Arbitrary Polyhedra Unstructured Grids," *AIAA Journal*, Vol. 51, No. 11, 2013, pp. 2740–2747. https://doi.org/10.2514/1.J052095

[27] Venkatakrishnan, V., "Convergence to Steady State Solutions of the Euler Equations on Unstructured Grids with Limiters," *Journal of Computational Physics*, Vol. 118, No. 1, 1995, pp. 120–130. https://doi.org/10.1006/jcph.1995.1084

[28] Jameson, A., and Turkel, E., "Implicit Schemes and LU Decompositions," *Mathematics of Computation*, Vol. 37, No. 156, 1981, pp. 385–397. https://doi.org/10.1090/S0025-5718-1981-0628702-9

[29] Hashimoto, A., Murakami, K., Aoyama, T., Yamamoto, K., Murayama, M., and Lahur, P. R., "Drag Prediction on NASA CRM Using Automatic Hexahedra Grid Generation Method," *Journal of Aircraft*, Vol. 51, No. 4, 2014, pp. 1172–1182. https://doi.org/10.2514/1.C032641

[30] Takayanagi, H., Yamada, K., Maru, Y., and Fujita, K., "Development of Supersonic Parachute for Mars EDL Demonstrator," *Proceedings of the 58th Space Sciences and Technology Conference*, Japan Soc. for Aeronautical and Space Sciences (JSASS) Paper JSASS-2014-4168, 2014 (in Japanese).

C. Pantano
Associate Editor